Materials Today Bio 29 (2024) 101298

Contents lists available at ScienceDirect

Materials Today Bio

journal homepage: www.journals.elsevier.com/materials-today-bio

Cuproptosis-based layer-by-layer silk fibroin nanoplatform-loaded PD-L1 siRNA combining photothermal and chemodynamic therapy against metastatic breast cancer

Zheng Li [a,b,1], Lan Cheng [a,1], Xiang Xu [a], Rui Jia [a], Siyu Zhu [a], Qian Zhang [a], Guotao Cheng [a], Baiqing Wu [a], Zulan Liu [a], Xiaoling Tong [a], Bo Xiao [a,**], Fangyin Dai [a,*]

[a] State Key Laboratory of Resource Insects, Key Laboratory for Sericulture Biology and Genetic Breeding, Ministry of Agriculture and Rural Affairs, College of Sericulture, Textile and Biomass Sciences, Southwest University, Chongqing, China
[b] National Agricultural Exhibition Center, China Agricultural Museum, Beijing, China

ARTICLE INFO

Keywords:
Cuproptosis
Layer-by-layer
Silk fibroin
PD-L1
Metastatic breast cancer

ABSTRACT

Cuproptosis is a newly identified form of copper-dependent cell death that differs from other known pathways. This discovery provides a new way to explore copper-based nanomaterial applications in cancer therapy. This study used a layer-by-layer self-assembling method to load $Cu_{2-x}S$ nanoparticle (NP) cores with the siRNA of the *PD-L1* immune escape-related gene and wrap a silk fibroin (SF) shell to form a multifunctional copper-based SF nanoplatform, denoted as CuS-PEI-siRNA-SFNs. CuS-PEI-siRNA-SFNs induced cuproptosis and exerted an antitumor effect via multiple mechanisms, including photothermal therapy (PTT), chemodynamic therapy (CDT), and immune activation. The presence of significant dihydrolipoamide *S*-acetyltransferase (DLAT) oligomers in 4T1 cells treated with CuS-PEI-siRNA-SFNs indicated the triggering of cuproptosis. Furthermore, *in vivo* experimental results showed that CuS-PEI-siRNA-SFNs efficiently accumulated in the tumor tissues of 4T1 tumor-bearing mice inhibited primary tumor and lung metastasis, and displayed excellent biosafety and antitumor activity. This study demonstrated that the synergistic effect of cuproptosis, PTT, CDT, and immune activation showed promise for treating metastatic breast cancer.

1. Introduction

Breast cancer significantly affects human health. The latest statistics by the American Cancer Society show that breast cancer is the most common cancer among women, accounting for 31 % of all new cases. Breast cancer accounts for up to 15 % of all cancer deaths in women, and metastasis is the leading cause of death. Breast cancer incidence in women slowly increases at about 0.5 % a year [1,2]. Chemotherapy remains the classic clinical choice for treating primary breast cancer and lung metastasis. However, cytotoxic chemotherapy drugs cannot target metastatic breast cancer, displaying poor therapeutic value and severe systemic side effects. The single chemotherapy treatment approach renders poor results for primary breast tumors and lung metastasis [3,4]. Therefore, exploring combined treatment strategies to inhibit metastatic breast cancer is essential.

Copper is an indispensable trace element in living organisms and is usually maintained at extremely low levels in mammals. However, cytotoxicity can occur when intracellular copper concentrations exceed the threshold for homeostasis. Tsvetkov et al. named this copper-dependent death cuproptosis, which is distinct from the known apoptosis, pyroptosis, necroptosis, and ferroptosis. Cuproptosis occurs via direct binding between copper and the lipoylated enzymes of the tricarboxylic acid (TCA) cycle, especially dihydrolipoamide *S*-acetyltransferase (DLAT). This leads to lipoylated protein aggregation and subsequent iron-sulfur cluster protein loss, causing protein-toxic stress and ultimate cell death. *Ferredoxin 1* (*FDX1*), the upstream regulator of mitochondrial protein lipoylation, is the key regulatory gene for cuproptosis and encodes a reductase that reduces Cu^{2+} to the more toxic Cu^{1+} form [5]. Xu et al. were the first to treat bladder cancer using a copper-based nanomaterial to induce cuproptosis, achieving excellent

* Corresponding author.
** Corresponding author.
E-mail addresses: bxiao@swu.edu.cn (B. Xiao), fydai@swu.edu.cn (F. Dai).
[1] These authors contribute equally to this work.

https://doi.org/10.1016/j.mtbio.2024.101298
Received 27 August 2024; Received in revised form 29 September 2024; Accepted 14 October 2024
Available online 16 October 2024

antitumor results in athymic mice with 5637 bladder tumors [6]. Lu et al. subsequently addressed platinum-based anticancer drug resistance using a copper-organic complex-based nanosystem [7]. Hu et al. developed stimulus-responsive copper complex nanoparticles that can efficiently deliver copper complex into cancer cells to induce cuproptosis [8]. Lu et al. developed a self-amplified cuproptosis nanoparticles (Cel-Cu NP) using celastrol (Cel), a natural product isolated from medical plant [9]. However, no studies involving cuproptosis induction using copper-based nanomaterials for treating metastatic breast cancer are available. The potential of cuproptosis and its synergistic effect with other anticancer pathways for treating metastatic breast cancer requires further exploration.

A nanoplatform was prepared using hollow mesoporous copper sulfide NPs ($Cu_{2-x}S$, $0 < x < 1$; CuS), a copper-based nanomaterial with a synergistic photothermal therapy (PTT) and chemodynamic therapy (CDT) effect. CuS, a P-type semiconductor material, displays a strong local surface plasmon resonance effect on near-infrared (NIR) radiation, exhibiting high photothermal conversion efficiency and good photothermal stability [10]. The copper released by CuS during NIR irradiation can produce hydroxyl free radicals (•OH) via the Haber-Weiss cycle redox reaction with the buffer matrix in the surrounding tumor environment for CDT [11,12]. High reactive oxygen species (ROS) concentrations cause oxidative damage to macromolecules such as DNA and protein, leading to tumor cell apoptosis, while high heat can improve ROS lethality in tumor cells [13–15]. In addition, although the hollow mesoporous CuS structure significantly increases its specific surface area and drug loading capacity, CuS displays poor tumor tissue targeting capacity, and some copper may leak out in advance. Moreover, since copper is an essential trace element in the human body and can be rapidly metabolized, further CuS modification is necessary [10,16,17]. This study aims to achieve sustained copper release by coating CuS with silk fibroin (SF) while loading PD-L1 siRNA into the NPs and combining these approaches with immunotherapy to increase antitumor efficacy.

The nanocore (CuS) was loaded with siRNA (siPD-L1) using a layer-by-layer self-assembly method to efficiently knock down *PD-L1* gene expression. *PD-L1* expression in tumor cells is considered essential in immune evasion since it promotes T-cell dysfunction and failure [18]. Strategies that inhibit *PD-L1* expression in tumor cells can reduce immune escape, reverse the immunosuppressive tumor microenvironment, and achieve immune activation, further increasing antitumor efficacy. $Cu_{2-x}S$-PEI NPs (CuS-PEI) are prepared by combining negatively charged CuS and positively charged PEI via electrostatic adsorption. The negatively charged siRNA is adsorbed to the PEI layer via electrostatic action to obtain $Cu_{2-x}S$-PEI-siRNA NPs (CuS-PEI-siRNA). However, because the siRNA exposed to the outermost layer is easily degraded and deactivated, an SF shell layer is added outside the CuS PEI-siRNA nanocore to

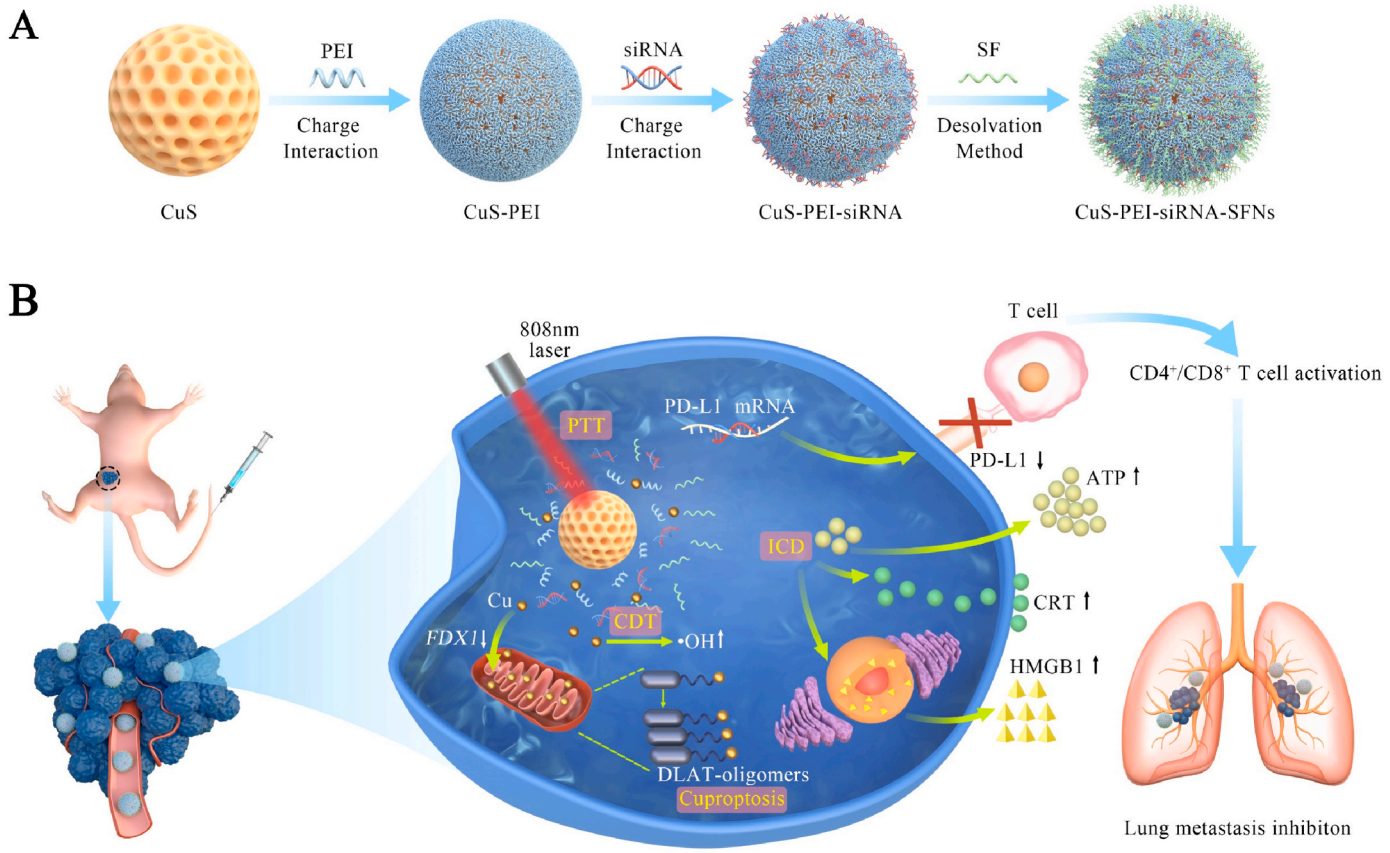

Fig. 1. A schematic illustration of the CuS-PEI-siRNA-SFNs preparation and its mechanism for metastatic breast cancer treatment. (A) The negatively charged porous CuS is adsorbed with PEI to prepare CuS-PEI via charge interaction. CuS-PEI-siRNA is obtained by loading siRNA on positively charged CuS-PEI via electrostatic adsorption. CuS-PEI-siRNA-SFNs are obtained by wrapping the CuS-PEI-siRNA nanocore in an SF shell using desolvation. (B) After entering 4T1 tumor cells, CuS-PEI-siRNA-SFNs facilitate PTT via NIR irradiation at 808 nm. The released PD-L1 siRNA binds to the PD-L1 mRNA and inhibits PD-L1 expression on the 4T1 cell membrane. This restricts PD-1 protein binding between the T cells and 4T1 cells and inhibits immune escape. Immunogenic death (ICD) occurs in the 4T1 cells. Considerable adenosine triphosphate (ATP) release significantly increases the extracellular ATP content and elevates CRT expression in the cell membrane. The HMGB1 proteins in the nucleus are secreted to the extracellular environment, increasing the extracellular HMGB1 content. In addition, Cu is released via CDT to produce •OH. The activated $CD4^+/CD8^+$ T cells and CuS-PEI-siRNA-SFN enrichment in the lungs inhibit breast cancer lung metastasis. The released Cu reduces *Ferredoxin 1* (*FDX1*) expression, regulating lipid-protein acylation and entering the mitochondria to directly bind with lipoylated DLAT. This caused DLAT oligomer formation, marking the occurrence of cuproptosis.

obtain SF-coated CuS-PEI-siRNA NPs (CuS-PEI-siRNA-SFNs). The outer layer of CuS-PEI-siRNA is coated with SF using a simple desolvation method. SF nanocarriers are simple to chemically modify and display excellent biocompatibility, multi-responsive sustained drug release, and degradability. Several studies have explored the application of SF nanosystems for cancer therapy [4,19–21]. The CuS-PEI-siRNA-SFNs SF shell protects the siRNA and sustains the copper, increasing the antitumor effect and reducing the toxic side effects. CuS-PEI-siRNA-SFNs can reduce breast cancer metastasis via quadruple-modal therapeutic strategies (cuproptosis, PTT, CDT, and immune activation) (Fig. 1).

2. Materials and methods

2.1. The layer-by-layer assembly preparation of the NPs

$CuCl_2{\cdot}2H_2O$ (136.4 mg) and polyvinylpyrrolidone (PVP, 800.0 mg) were dissolved in 400 mL of deionized water and stirred for 5 min. Then, a 16 mL NaOH (0.2 M) solution was added dropwise for 5 min, followed by 16 mL of 0.1 M L-ascorbic acid. The mixture was continuously stirred at room temperature for 5 min, followed by the dropwise addition of 16 mL of a Na_2S aqueous solution (1.0 M), which immediately turned black and continued to be stirred in a water bath at 60 °C for 3 h. The unreacted impurities were removed three times via centrifugation step (10000 g, 10 min) to obtain the $Cu_{2-x}S$ NPs (CuS).

CuS suspension (5 mL, 8 mg/mL) was added dropwise to an equal concentration and volume of PEI aqueous solution and stirred for 15 min. The solution was washed three times, after which the CuS_{2-x}-PEI NPs (CuS-PEI) were collected. The $Cu_{2-x}S$-PEI-siRNA NPs (CuS-PEI-siRNA) were obtained by gently mixing siPD-L1 (20 μM) with CuS-PEI at a ratio of 1:250 (w/w).

The CuS-PEI-siRNA suspension (2 mL, 8 mg/mL) was dispersed in a 30 mL acetone solution, after which a 3 mL SF solution (5 mg/mL) was added dropwise and stirred until the acetone had completely volatilized. The SF-coated CuS-PEI-siRNA NPs (CuS-PEI-siRNA-SFNs) were collected via centrifugation at 13,000 g for 10 min, washed three times with water, and ultrasonically treated in an ice bath for 1 min (195 W).

2.2. Chemodynamic assay

CuS, CuS-PEI-siRNA, and CuS-PEI-siRNA-SFNs suspensions (950 μL, equivalent to 50 μg/mL Cu) were mixed with 50 μL 2′,7′-dichlorodihydrofluorescein (DCFH, 20 μmol/mL) and placed in 2 mL centrifuge tubes. After NIR irradiation (808 nm) for 5 min (2 W/cm^2), the supernatants were collected via centrifugation at 12000*g* for 5 min. The ROS generated by the NPs via chemical kinetics reacted with the DCFH to produce fluorescent DCF. The fluorescence intensity in each supernatant was detected using a microplate reader (Synergy H1, Biotek, USA) (λ_{ex} = 488 nm, λ_{em} = 525 nm) to compare the ability of various NPs to produce ROS *in vitro*.

The intracellular ROS levels were detected using a DCFH-diacetate (DCFH-DA) Reactive Oxygen Species detection kit (Beyotime, China). Next, 4T1 cells were seeded into 12-well plates containing cell slides at a density of 1 × 10^5 cells per well. After culturing for 24 h at 37 °C, the original medium was changed to the serum-free medium containing CuS, CuS-PEI-siRNA, and CuS-PEI-siRNA-C6-SFNs (equivalent to 5 μg/mL Cu) for 4 h. Then, the NIR irradiation group cells were irradiated (808 nm, 2 W/cm^2) for 3 min and incubated for 1 h. After discarding the original medium, the mixture was washed three times with PBS, after which pre-diluted DCFH-DA was added and incubated for 30 min. The cells were fixed with 4 % paraformaldehyde for 10 min and examined using confocal laser scanning microscopy (CLSM, FV3000, Olympus, Japan).

2.3. The in vitro anticancer activity of the NPs

Here, 4T1 cells were seeded in 96-well cell plates at a density of 7.5 × 10^3 for 24 h. The original medium was replaced with the basic medium containing gradient CuS, CuS-PEI-siRNA, and CuS-PEI-siRNA-SFNs concentrations, while the NPs-free group was used as the control group. The NIR irradiation group cells were treated with various samples for 4 h, irradiated (808 nm, 2 W/cm^2) for 3 min, and incubated for 24 h. Then, the medium was removed, and the well plate was cleaned three times with PBS to remove residual drugs or NPs. Then, 100 μL of culture medium containing 10 % CCK8 reagent (TransGen Biotech, China) was added to each well and incubated at 37 °C for 1 h. The OD value of each well and the cell viability were determined at 450 nm using a microplate analyzer.

To investigate the influence of cuproptosis inhibitors on the CuS and CuS-PEI-siRNA-SFNs cytotoxicity, 4T1 cells were pre-treated with cupper chelator (disodium bathocuproinedisulfonate, (BCS), 25–75 μM) for 8 h. Then CuS and CuS-PEI-siRNA-SFNs were added (equivalent to 30 μg/mL Cu). The NIR irradiation group cells were treated with different samples for 4 h, irradiated (808 nm, 2 W/cm^2) for 3 min, and cultured for another 20 h. After 20 h culturing, they were subjected to CCK8 cell viability measurements.

2.4. Analysis of the gene expression and western blotting in vitro

Here, 4T1 cells were seeded into 12-well cell plates at a density of 2 × 10^5 for 24 h. The original medium was replaced with a basic medium containing CuS, CuS-PEI-siRNA, and CuS-PEI-siRNA-SFNs (equivalent to 5 μg/mL Cu), while the group containing no NPs was used as the control. The NIR irradiation group cells were treated with various samples for 4 h, irradiated (808 nm, 2 W/cm^2) for 3 min, and incubated for another 20 h. After 24 h culturing, the medium was removed, and the well plate was cleaned three times with PBS. Then, 800 μL lysate or 200 μL RIPA lysis buffer was added to each well for total RNA and protein extraction. The RNA was reverse transcribed into cDNA and detected using real-time fluorescence quantitative PCR. β-actin was selected as the reference gene and detected using a real-time PCR system (Bio-Rad, USA). The primers used for the quantitative real-time polymerase chain reaction (QPCR) are shown in Table S2. The protein concentrations were determined using a BCA kit (Beyotime, China). The proteins were separated via 10 % SDS-PAGE and transferred to PVDF membranes. After blocking with 5 % skim milk powder/TBST, the membranes were incubated overnight with specific primary antibodies at 4 °C. The primary antibodies were washed with TBST and incubated with the horseradish peroxidase-labeled secondary antibody. Finally, a western ECL substrate (Bio-Rad, USA) was employed for imaging using a gel imaging analysis system (ChemiDoc™ Touch, Bio-Rad, USA). The antibodies used in this experiment included anti-DLAT (Absmart, T58125S, 1:2000) and anti-β-actin (Absmart, P30002S, 1:2000).

2.5. The induction of immunologic cell death (ICD)

To investigate NP-induced tumor cell ICD, the HMGB1, ATP, and CRT surface exposure were examined *in vitro*. For released HMGB1 and ATP detection, 4T1 cells were seeded into 12-well cell plates at a density of 2 × 10^5 for 24 h. Then, the cells were treated with CuS-PEI-siRNA and CuS-PEI-siRNA-SFNs (50 nM siPD-L1) for 24 h. The NIR irradiation group cells were treated with various samples for 4 h, irradiated (808 nm, 2 W cm^{-2}) for 3 min, and incubated for 20 h. The supernatant was collected to measure the ATP and HMGB1 concentrations using ATP assay kits and HMGB1 ELISA kits (Beyotime, China), respectively, according to the instructions of the manufacturer. The lysed cytosol was collected for intracellular ATP detection, while the *PD-L1* gene expression in treated cells was determined via QPCR.

Immunofluorescence was used to examine the CRT. Here, 4T1 cells were seeded into 12-well cell plates at a density of 1 × 10^5 for 24 h. The cells were treated with CuS-PEI-siRNA and CuS-PEI-siRNA-SFNs (50 nM siRNA) for 24 h, after which they were cleaned three times with PBS. Next, the cells were fixed with 4 % paraformaldehyde for 15 min,

blocked for 1 h at room temperature, and incubated overnight with the primary anti-CRT antibody (1:200) at 4 °C. The cells were then incubated with the secondary Alexa Fluor 488-conjugated antibody (1:1000) for 1 h at room temperature, stained with DAPI, and visualized using CLSM (FV3000, Olympus, Japan). The fluorescence intensity of the CRT was quantitatively analyzed using the Image J software.

2.6. The in vivo evaluation of the anticancer outcomes and lung metastasis inhibition

The tumor model was established by subcutaneously injecting 5×10^5 4T1 cells onto the dorsa of female BALB/C Nude mice (5–6 weeks old). The tumor volumes were calculated using the following formula: Tumor volume = $L \times W^2/2$. L and W represented the length and width of the tumors, respectively. The tumor-bearing mice with tumor volumes of about 100 mm^3 were divided into eight groups, including the PBS control group, the PBS (+NIR)-treated group, the CuS-treated group, the CuS (+NIR)-treated group, the CuS-PEI-siRNA-treated group, the CuS-PEI-siRNA (+NIR)-treated group, the CuS-PEI-siRNA-SFNs-treated group, and the CuS-PEI-siRNA-SFNs (+NIR)-treated group. The mice in the various drug-treated groups were administered with PBS (200 μL) and various NPs at an equivalent dose of 5 mg/kg Cu (200 μL) once daily for a total of three doses. The tumors in the irradiated mouse groups were exposed to an 808 nm laser 24 h after injection at a power density of 0.8 W/cm^2 for 5 min. Their body weights and tumor volumes were recorded every 3 d throughout the experiment.

At the end of the experiment, the tumors were collected, photographed, and the final weight was recorded, after which they were fixed in 4 % paraformaldehyde and embedded in paraffin. The tissue sections (5 μm) were stained using H&E, Ki67, and TUNEL kits, respectively. The Cu content of the tumors and main organs in the various drug-treated groups was measured using inductively coupled plasma optical emission spectrometry (ICP-OES, Thermo-7200, Thermo Fisher, USA). The activated $CD4^+$ and $CD8^+$ T cells in the tumor tissue were identified via immunofluorescence staining. The total RNA of the tumors was extracted via RIPA lysis and quantified using QPCR analysis to determine the *FDX1* gene expression after different treatments. The *PD-L1* expression in the tumor microenvironment was examined using immunohistochemistry. Furthermore, the lungs of the different treatment groups were harvested to visualize and count the tumor metastasis nodules, while lung slices were stained with H&E for the pathological lung metastasis assay.

2.7. Statistical analysis

The statistical significance of the data differences was evaluated using Student's *t*-test or one-way ANOVA. The statistical significance was represented by $^*P < 0.05$, $^{**}P < 0.01$, and $^{***}P < 0.001$. The data were expressed as the mean ± standard error of the mean (S.E.M).

3. Results and discussion

3.1. The construction and physicochemical characterization of the NPs

The CuS was obtained using a facile two-step synthesis procedure [22–24]. This involved the formation of Cu_2O spheres, which were converted into CuS. Then, CuS-PEI and CuS-PEI-siRNA were obtained using the layer-by-layer assembly method [25,26]. Next, CuS-PEI-siRNA-SFNs were prepared via the desolvation of SF NPs (SFNs) [4,20,27]. Dynamic light scattering (DLS) was used to determine the particle size, polydispersity index (PDI), zeta potential, drug release performance, cell uptake efficiency, and biological distribution of the NPs, which were vital stability parameters [28]. As shown in Table S1, the CuS displayed a particle size of 120.4 nm and a zeta potential of −16.4 mV. Positively charged PEI was adsorbed on the CuS surface via electrostatic interaction, positively charging the CuS-PEI surface (+20.0 mV). The negatively charged siPD-L1 continued to be deposited on the CuS-PEI surface via electrostatic adsorption. This process used siPD-L1-3, which exhibited the highest *PD-L1* gene silencing efficiency of the three siRNA pairs obtained via transfection and detection in the 4T1 cells (Fig. S1).

The nanocore was assembled via electrostatic action between the CuS-PEI and siRNA at a mass ratio of 250:1. The siRNA was totally absorbed (Fig. S2), forming a spheroidal nanocore with a particle size of 120.2 nm and a zeta potential of +8.8 mV. The siRNA could not be completely adsorbed by the CuS-PE at a mass ratio below 250:1, resulting in waste, while the siRNA loading rate in the NPs decreased at a mass ratio exceeding 250:1. Therefore, a ratio of 250:1 (CuS-PEI:siRNA) was selected as optimal for preparation. Zeta potential analysis after the deposition of each layer revealed a reversal and change in the surface charge, marking PEI and siRNA deposition on the NPs (Fig. 2B). Scanning electron microscopy (SEM) and transmission electron microscopy (TEM) showed that the CuS, CuS-PEI, and CuS-PEI-siRNA presented spherical structures with uniform particle size distribution (Fig. 2A). The particle size discrepancy between the SEM/TEM and DLS results could be because the NPs were shrunken during the TEM observation, while they were swollen in an aqueous solution during the DLS tests [20,29].

An SF solution was added to the acetone mixture containing CuS-PEI-siRNA. As a polar protic solvent, the acetone destroyed the water molecular layer of the SF and promoted the SF chain aggregation via hydrophobic interaction. Moreover, the aggregated SF chains shrank and self-assembled due to hydrophobic pressure, encapsulating the CuS-PEI-siRNA inside to form CuS-PEI-siRNA-SFNs [21,27]. The PDIs of these NPs were <0.2, highlighting their limited size distribution (Table S1). In addition, the SF shell structure (Fig. 2A) wrapped in the outer layer of CuS-PEI-siRNA was clearly observed via TEM. Furthermore, SEM showed that the CuS-PEI-siRNA-SFNs particles were significantly larger than CuS-PEI-siRNA, with slightly irregular morphological characteristics. The hydrated CuS-PEI-siRNA-SFNs (218.8 nm) particles were significantly larger than CuS-PEI-siRNA (120.2 nm), while the charge changed from positive (+8.8 mV) to negative (−29.8 mV). It also indicated the successful SF inclusion on the CuS-PEI-siRNA (Fig. 2A and B). SF shell formation protected the siRNA and allowed sustained Cu release. The ICP-OES results showed that Cu drug loading rate was 76.6 % in CuS and 64.9 % in CuS-PEI. The Cu drug loading rate in CuS-PEI-siRNA continued to decrease to 57.3 % due to the limited copper leakage caused by PEI chelation with copper ions. The Cu drug loading rate was the lowest (30.2 %) in the CuS-PEI-siRNA-SFNs after SF addition, indicating successful SF deposition on the nanocore surface. In addition, as shown in Fig. S21, the particle size of CuS-PEI-siRNA-SFNs did not change significantly within 3 days in PBS and DMEM, indicating that the nanoparticles had good stability.

The NPs were subjected to full spectrum scanning to further determine the CuS and SF core-shell structures. As shown in Fig. 2C, the SFNs displayed an absorption peak at 280 nm. Compared to CuS-PEI-siRNA, the CuS-PEI-siRNA-SFNs spectrum changed at about 280 nm, indicating successful SF and CuS-PEI-siRNA self-assembly. In addition, the Fourier transform infrared spectroscopy (FTIR) images showed that the SFNs displayed characteristic amide I (1636 cm^{-1}), amide II (1530 cm^{-1}), and amide III (1235 cm^{-1}) absorption peaks (Fig. 2D). The CuS-PEI-siRNA-SFNs also exhibited these three characteristic peaks, while no corresponding peaks were evident for CuS and CuS-PEI. These characteristic peaks represented the typical SF β-sheet structure, indicating that the SFNs were mainly present in the Silk II crystalline structure [20,30]. In addition to SFNs, the CuS-PEI-siRNA-SFNs, and the other three NPs all displayed a characteristic peak at 615 cm^{-1}, which corresponded to tensile Cu-S bond vibration, indicating successful copper sulfide synthesis and the presence of CuS in the NPs.

X-ray photoelectron spectroscopy (XPS) was used to investigate the elemental composition and chemical valence state of the Cu in the CuS-PEI-siRNA-SFNs (Fig. 2E), primarily identifying five elements: C, N, O, Cu, and S (Fig. S4). Cu and S provided the basis for successful CuS

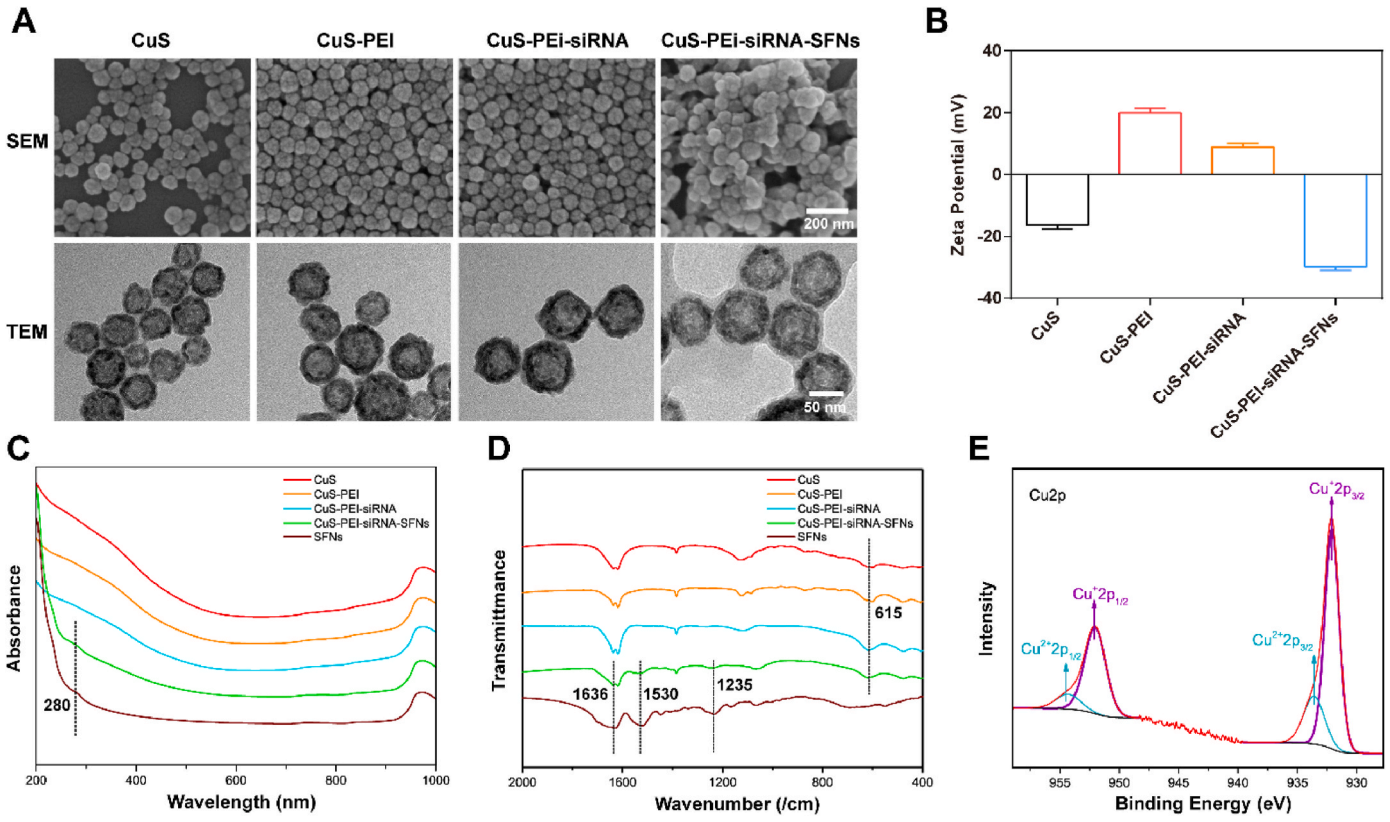

Fig. 2. The morphological and structural characterization of the NPs. (A) The SEM and TEM images of CuS, CuS-PEI, CuS-PEI-siRNA, and CuS-PEI-siRNA-SFNs. (B) The zeta potential of CuS, CuS-PEI, CuS-PEI-siRNA, and CuS-PEI-siRNA-SFNs. (C) The full spectrum scanning peak image of the SF and NPs. (D) The FTIR images of the SF and NPs. (E) The XPS spectra of the CuS-PEI-siRNA-SFNs. The error bars represent the mean ± S.E.M.

synthesis. C and N were derived from PEI, siRNA, and SF, while O was obtained from siRNA and SF. The Cu 2p peaks at 933.6 eV and 954.3 eV corresponded to the Cu (II) state, while those at 932.1 eV and 952.0 eV were associated with the Cu (I) state. XPS quantitative analysis showed that Cu (I) accounted for 78.7 %, and Cu (II) represented 21.3 %. These results suggested that Cu (I) and Cu (II) co-existed in CuS [31]. Since Cu (I) displayed higher toxicity than Cu (II) during cuproptosis, the high Cu (I) level in the CuS-PEI-siRNA-SFNs promoted the antitumor impact [5].

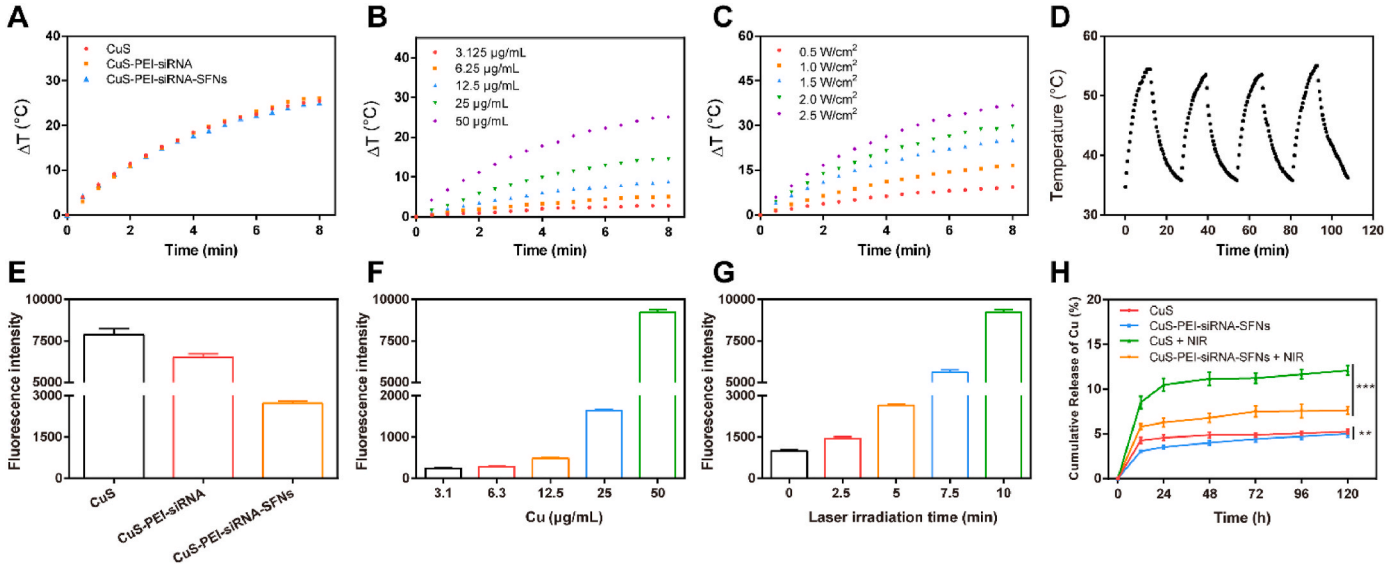

Fig. 3. The physicochemical characterization of the NPs. (A) The photothermal heating curve of CuS, CuS-PEI-siRNA, and CuS-PEI-siRNA-SFNs (equivalent to 50 μg/mL Cu,1.5 W/cm^2). (B and C) The photothermal heating curve of the CuS-PEI-siRNA-SFNs. (D) The temperature variations in the suspension exposed to NIR laser irradiation (1.5 W/cm^2) for four cycles. (E) The fluorescence intensity of the detected extracellular ROS produced by different NPs after NIR laser irradiation (2 W/cm^2, 5 min). (F and G) The fluorescence intensity of the detected extracellular ROS produced by CuS-PEI-siRNA-SFNs at different Cu concentrations and NIR laser power values. (H) The cumulative release profiles of the Cu from the CuS and CuS-PEI-siRNA-SFNs in PBS (pH 7.4). The error bars represent the mean ± S.E.M (n = 3).

3.2. The photothermal profiles of the NPs

The CuS converted light energy into heat energy when exposed to an NIR laser and was used to examine the photoactivity and photostability of CuS, CuS-PEI-siRNA, and CuS-PEI-siRNA-SFNs. As shown in Fig. 3A, when irradiated for 8 min at a power density of 1.5 W/cm^2, the temperature of each NP suspension increased as the irradiation time was extended. Moreover, no significant differences were evident between the photothermal temperature curves of the CuS, CuS-PEI-siRNA, and CuS-PEI-siRNA-SFNs (equivalent Cu concentration: 50 μg/mL), indicating that the self-assembled PEI and siRNA layers and SF shell encapsulation did not affect the photothermal effect of CuS. At 1.5 W/cm^2 irradiation, the temperature CuS-PEI-siRNA-SFNs suspension increased at a higher NP concentration, indicating that the temperature was proportional to the concentration (Fig. 3B) In addition, the temperature-rise profiles of the CuS-PEI-siRNA-SFNs suspension also increased at a higher laser irradiation power (Fig. 3C). Therefore, 50 μg/mL of CuS-PEI-siRNA-SFNs could be heated to 64.3 °C at 808 nm laser (2 W/cm^2) irradiation for 8 min. These results indicated that the photothermal effect of the CuS-PEI-siRNA-SFNs suspension was time-, concentration-, and power-dependent. The CuS produced a local surface plasmon resonance effect after NIR irradiation, representing the main mechanism behind the CuS photothermal ability [32,33]. To determine the photothermal stability of the CuS-PEI-siRNA-SFNs, their temperature peak fluctuations during the irradiation cycle were evaluated (Fig. 3D). After each laser irradiation, the dispersion temperature rose to 54.4 °C, 53.5 °C, 53.5 °C, and 55 °C, respectively. The peak temperature values of the CuS-PEI-siRNA-SFNs remained the same throughout irradiation. This indicated that the temperature changes caused by specific irradiation cycles did not change the photothermal heating effect of CuS-PEI-siRNA-SFNs. In addition, the full-spectrum scanning pattern of CuS-PEI-siRNA-SFNs did not change before and after four exposures (Fig. S5). The photothermal conversion efficiency was an important feature of the nano photothermal materials. The photothermal conversion efficiency of the CuS-PEI-siRNA-SFNs reached 52.1 % (Fig. S6), indicating their excellent photothermal effect and stability.

3.3. Cu release and extracellular ROS generation

The Cu release in the CuS and CuS-PEI-siRNA-SFNs was examined since it was critical for ROS generation and cuproptosis. The Cu release rate from CuS was significantly faster than the CuS-PEI-siRNA-SFNs in PBS (pH 7.4) (Fig. 3H). The same phenomenon was observed in NIR irradiation conditions, mainly because the SF shell delayed and sustained Cu release. Furthermore, when exposed to NIR irradiation, the Cu release from CuS and CuS-PEI-siRNA-SFNs was significantly higher than from the group without irradiation. This may be due to higher levels of CuS solubility products (*K*sp) at high temperatures when exposed to laser irradiation, accelerating Cu release [12]. These results indicated that the heat generated by NIR irradiation promoted Cu release, which encouraged ROS generation and cuproptosis.

To explore whether the prepared NPs displayed the chemical kinetic ability to produce ROS, DCFH was used as a fluorescent ROS probe outside the cells to determine whether the prepared NPs displayed the chemical kinetic ability to produce ROS. When produced, the ROS interacted with DCFH to generate fluorescent 2′,7′-dichlorofluorescein (DCF, λex = 488 nm, λem = 525 nm). The DCF fluorescence intensity values were used to compare the ability of each NPs to produce ROS *in vitro*. The ROS production was mainly attributed to Cu leakage from CuS when exposed to NIR irradiation, generating •OH via the redox reaction during the Haber-Weiss cycle [11]. The CuS yielded the highest fluorescence intensity, followed by the CuS-PEI-siRNA and CuS-PEI-siRNA-SFNs, which was primarily due to the release of Cu in the NP suspensions after irradiation. The results (Fig. 3H) showed that the Cu release by the CuS-PEI-siRNA-SFNs after irradiation was significantly lower than CuS, reducing subsequent ROS production. Compared with CuS, the CuS-PEI-siRNA surface was coated with PEI and siRNA layers, possibly affecting Cu release and reducing ROS production. In addition, higher fluorescence intensity was evident as the NIR irradiation duration and Cu concentration in the CuS-PEI-siRNA-SFNs increased (Fig. 3F and **G)**. This indicated that the ROS production by the CuS-PEI-siRNA-SFNs exposed to NIR irradiation *in vitro* was time- and concentration-dependent. These results demonstrated that the CuS-PEI-siRNA-SFNs displayed excellent PTT and ROS generation ability *in vitro*.

3.4. The in vitro cellular NP uptake and intracellular ROS generation

Green fluorescing C6-labeled CuS-PEI-siRNA-C6-SFNs were prepared to determine their ability to enter 4T1 cells, and their behavior was examined via CLSM and flow cytometry (FCM). The CuS-PEI-siRNA-C6-SFNs were incubated with 4T1 cells for 1 h (Fig. 4A), they entered the 4T1 cell cytoplasm and did not distribute in the nucleus. This indicated the successful uptake of the CuS-PEI-siRNA-C6-SFNs by the 4T1 cells. Although a small amount of fluorescence overlapped with the nucleus after incubation for 2 h, the fluorescence was mostly distributed in the cytoplasm. However, after incubation for 4 h, more fluorescence was evident in the nucleus than in the cytoplasm, possibly due to the release of some C6 from the CuS-PEI-siRNA-C6-SFNs into the nucleus. In addition, the FCM results (Fig. 4C) showed that the uptake rate of 4T1 cells increased significantly to 40.9 % after CuS-PEI-siRNA-C6-SFNs treatment for 1 h. After co-incubation for 2 h and 4 h, the uptake rate of the cells increased to 76.9 % and 96.9 %, respectively. As shown in Fig. S7, the average fluorescence intensity (MFI) was higher at 4 h than at 1 h and 2 h, while the CuS-PEI-siRNA-C6-SFNs uptake increased as the incubation duration was extended. Therefore, the CuS-PEI-siRNA-C6-SFNs uptake by the 4T1 cells was time-dependent. Furthermore, ICP-OES was used to quantify the Cu uptake content in each cell. The Cu uptake was 0.8 pg/cell after CuS-PEI-siRNA-C6-SFNs and 4T1 incubation for 1 h, increasing to 1.5 pg/cell and 2.4 pg/cell, respectively, after co-incubation for 2 h and 4 h. Therefore, the Cu uptake from the CuS-PEI-siRNA-C6-SFNs by the 4T1 cells was also time-dependent. Moreover, the CuS-PEI-siRNA-C6-SFNs Cu content initially added to the 4T1 cells was marked as 100 % to convert the Cu uptake rate in 4T1 cells, which reached 62.0 % after 4 h of co-incubation (Fig. S8). Overall, the CuS-PEI-siRNA-C6-SFNs and its loaded Cu were efficiently taken up by the 4T1 cells, which was critical for killing tumor cells via cuproptosis.

High ROS concentrations can denature macromolecules such as DNA and protein, leading to tumor cell apoptosis [13–15]. Since the results (Fig. 3) indicated that CuS, CuS-PEI-siRNA, and CuS-PEI-siRNA-SFNs produced ROS outside the cell, the ability of these NPs to produce ROS inside the cell was investigated. DCFH-DA was used to determine the intracellular ROS level. As a ROS probe, DCFH-DA easily crosses the cell membrane to enter the cell, where it is hydrolyzed by cellular esterase to produce DCFH, which further reacts with ROS to produce DCF with green fluorescence. As shown in Fig. S9, no green fluorescence was evident in the control group with or without exposure to NIR irradiation. In the absence of NIR irradiation, the CuS, CuS-PEI-siRNA, and CuS-PEI-siRNA-SFNs exhibited green fluorescence due to minimal Cu leakage from the NPs, producing a small amount of ROS. The protection provided to the CuS-PEI-siRNA-SFNs by the SF shell restricted Cu leakage, consequently yielding the lowest fluorescence. When exposed to NIR irradiation, the green fluorescence of the three NP groups was stronger than the corresponding non-irradiated groups. This indicated that the three NP groups produced high ROS levels in the 4T1 cells after NIR irradiation, which could be used for tumor CDT.

3.5. The in vitro anticancer effect and ICD induction of NPs

To determine the NP toxicity on the 4T1 cells, The CuS, CuS-PEI-siRNA, and CuS-PEI-siRNA-SFNs were incubated with the 4T1 cells for 24 h and detected using the CCK8 method. As shown in Fig. 5A, at a Cu

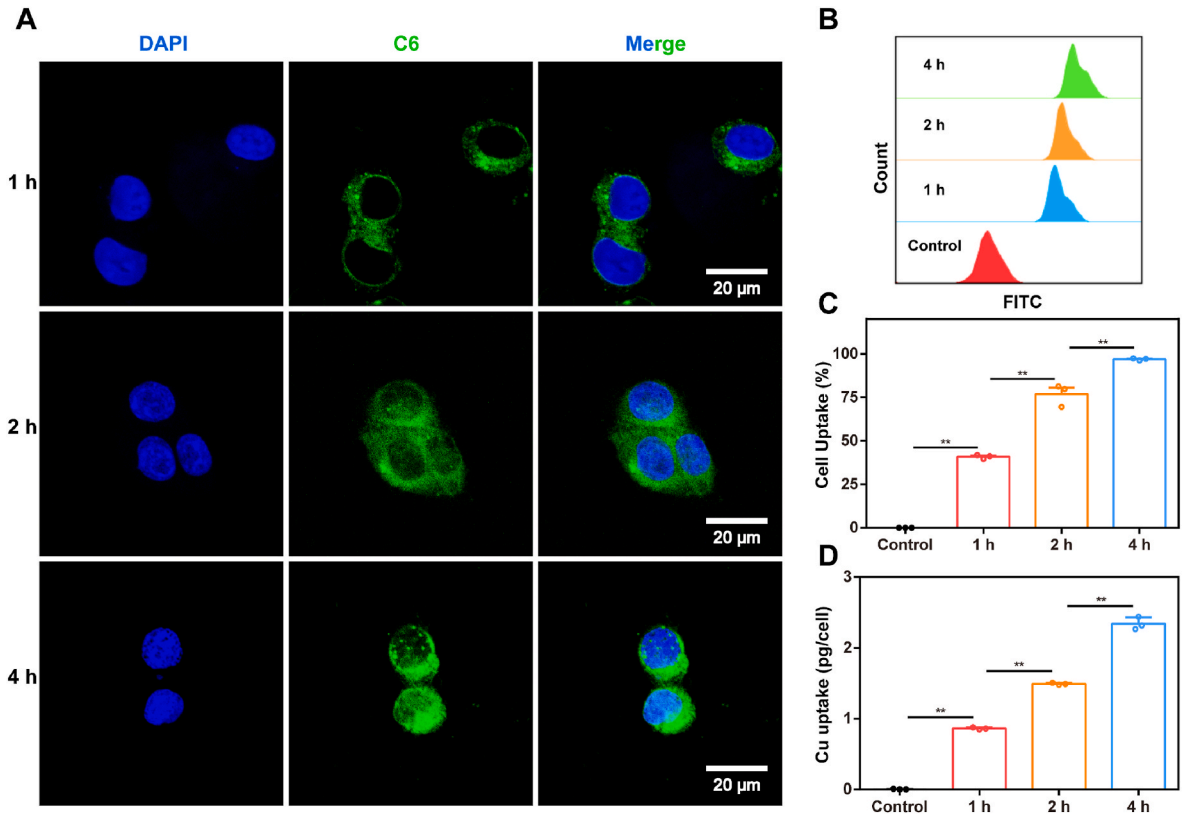

Fig. 4. The 4T1 cell uptake profiles of the NPs and Cu. (A) The CuS-PEI-siRNA-C6-SFNs distribution in the 4T1 cells was observed via CLSM after incubation with F-P-D-S for 1 h, 2 h, and 4 h. The F-P-D-S was observed via the green fluorescence of C6 (FITC channel). (B) After CuS-PEI-siRNA-C6-SFNs and 4T1 cell incubation for 1 h, 2 h, and 4 h, the 4T1 cell fluorescence intensity distribution was analyzed using FCM. Cells without NP treatment were set as a control. (C and D) The statistics of the cellular uptake rate and Cu uptake of the CuS-PEI-siRNA-C6-SFNs after incubation with the 4T1 cells for 1 h, 2 h, and 4 h. The error bars represent the mean ± S.E.M (**$P < 0.01$, n = 3).

concentration of 5 μg/mL in CuS, the NIR treatment group displayed toxicity toward the 4T1 cells than the non-irradiated group, while the cytotoxic differences between these groups were more pronounced at a 10 μg/mL Cu concentration. When the Cu concentration in CuS was increased to 20 μg/mL, the cytotoxic differences between the irradiated and non-irradiated groups decreased since the cytotoxicity caused CuS cuproptosis in non-irradiated conditions was already exceedingly high, and the additional toxicity caused by PTT and CDT became less obvious. Fig. 5B and **C** showed a similar trend. No significant differences were evident between the 4T1 cell toxicity of CuS, CuS-PEI-siRNA, and CuS-PEI-siRNA-SFNs loaded with the same amount of Cu, regardless of whether they were exposed to NIR irradiation. Furthermore, the cytotoxicity of these three NPs to normal cells (L929) with or without exposure to NIR irradiation was investigated. As shown in Fig. S10, no significant differences were apparent between the NP cell toxicity in irradiated and non-irradiated conditions, possibly because the normal cells were more tolerant to irradiation and heat than tumor cells [34]. Furthermore, at NP Cu levels of 20 μg/mL and 40 μg/mL, the viability of the L929 cells in the CuS-PEI-siRNA-SFNs treatment group was significantly higher than those in the CuS- and CuS-PEI-siRNA-treated groups. At high Cu concentrations (20 μg/mL and 40 μg/mL), the L929 cell viability in the CuS-PEI-siRNA-SFNs-treated group was significantly higher than the 4T1 cells. This indicated that the CuS-PEI-siRNA-SFNs displayed selective cytotoxic inhibition and a potential biosafety capacity.

To confirm the role of cuproptosis in NP-mediated cell death, the cuproptosis inhibitor, disodium BCS, was treated with CuS or CuS-PEI-siRNA-SFNs to determine cell viability. As shown in Fig. 5D, in non-irradiated and NIR irradiation conditions, the cell viability was about 100 % after free BCS treatment, indicating that BCS displayed no cytotoxicity toward 4T1 cells within the experimental concentration range. However, the cell viability was significantly higher in the BCS + CuS-treated group than in the CuS-treated group since the chelation between BCS and the Cu released from CuS significantly inhibited cuproptosis. The multifold cell viability cell change after co-treatment was compared with non-inhibitor treatment to elucidate the effect of the cuproptosis inhibitor (Fig. 5E). The BCS to CuS cell viability reversal ratio increased gradually at a higher BCS concentration. Similarly, a significant reversal was evident in the CuS-PEI-siRNA-SFNs cytotoxicity when combined with BCS. However, the reversal magnitude in the combined CuS-PEI-siRNA-SFNs treatment group was lower than in the combined CuS treatment group, possibly due to the sustained release of Cu from CuS-PEI-siRNA-SFNs. The Cu release was lower in CuS-PEI-siRNA-SFNs than in CuS over 24 h, allowing a small amount of BCS to fully chelate the Cu. Therefore, the reversal ratio of the combined CuS-PEI-siRNA-SFNs treatment group did not increase significantly, even at higher BCS concentrations.

Western blotting was used to analyze and detect the oligomerization of the cuproptosis marker protein (DLAT) in each treatment group to verify the occurrence of cuproptosis (Fig. 5F) [5,6]. No significant DLAT oligomers were found in the first two lanes of the control group without NP treatment. Obvious DLAT oligomers were evident in all the NP-treated groups loaded with Cu. Furthermore, the expression of another cuproptosis marker gene (*FDX1*) was also detected via QPCR, representing the upstream regulator of protein lipid acylation in the mitochondria (Fig. S11) [5,7]. The *FDX1* gene expression in the various NP-treated groups was significantly down-regulated, suggesting that these NPs triggered cuproptosis in 4T1 cells. These results indicate that CuS, CuS-PEI-siRNA, and CuS-PEI-siRNA-SFNs can effectively kill 4T1 cells via cuproptosis.

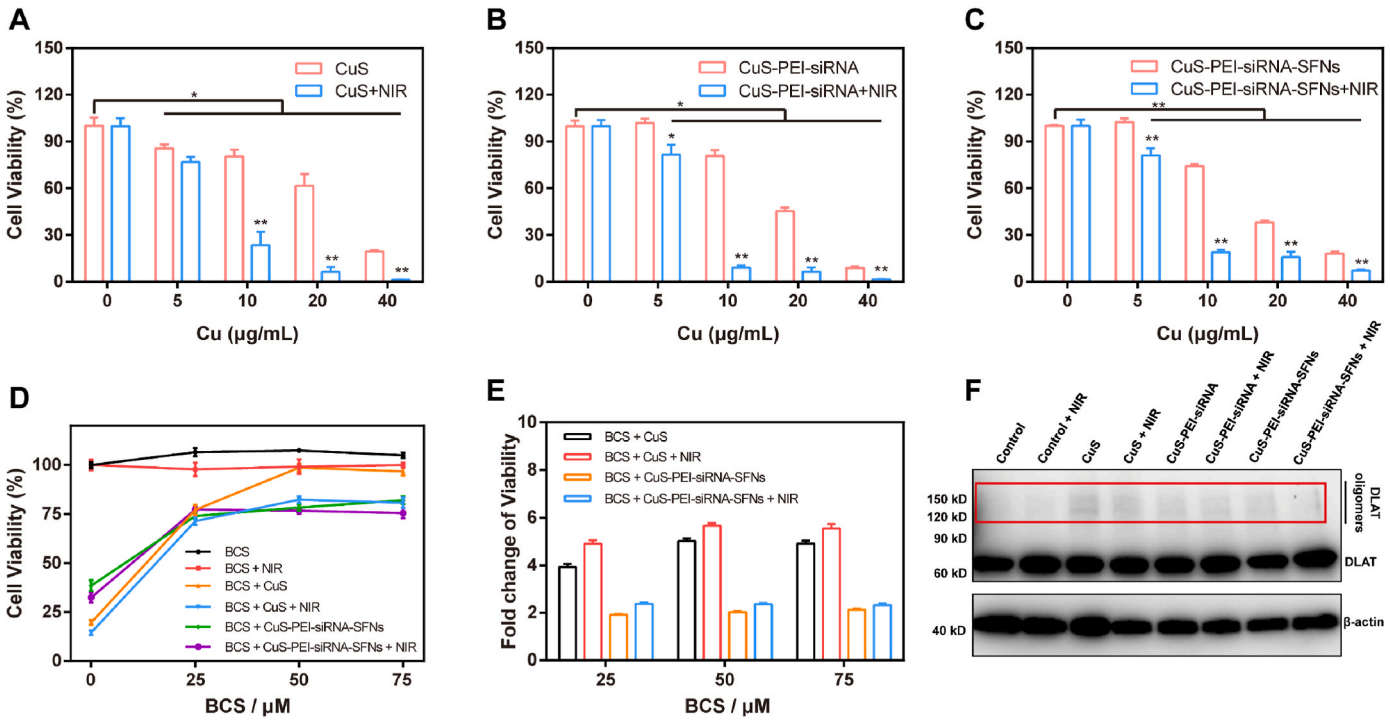

Fig. 5. The cytotoxicity and cuproptosis analysis of the NPs in the 4T1 cells. (A, B, and C) The cell viability of the 4T1 cells treated with CuS, CuS-PEI-siRNA, and CuS-PEI-siRNA-SFNs with or without NIR irradiation (2 W/cm^2, 3min). (D and E) The cell viability of the 4T1 cells pre-treated with the BCS cuproptosis inhibitor at different concentrations, followed by CuS and CuS-PEI-siRNA-SFNs treatment with or without NIR irradiation (2 W/cm^2, 3 min). (F) The 4T1 cells were analyzed for DLAT oligomerization after CuS and CuS-PEI-siRNA-SFNs treatment with or without NIR irradiation (2 W/cm^2, 3min). Cells without NP treatment were set as the controls. The error bars represent the mean ± S.E.M. The significance mark on the error bar is the result of comparison between groups with or without NIR. (*P < 0.05 and **P < 0.01, n = 3).

The mRNA expression levels of *CD274* (gene encoding PD-L1) were quantified using a quantitative QPCR assay to investigate the gene silencing effect of the NPs on the PD-L1 in the 4T1 cells. Incubation with CuS-PEI-siRNA and CuS-PEI-siRNA-SFNs significantly inhibited the *PD-L1* gene expression in the 4T1 cells, which was reduced to 40.9 % and 35.3 %, respectively, compared to the control group. When exposed to NIR irradiation, the *PD-L1* gene expression levels in the CuS-PEI-siRNA-treated and CuS-PEI-siRNA-SFNs-treated groups were reduced to 46.1 %

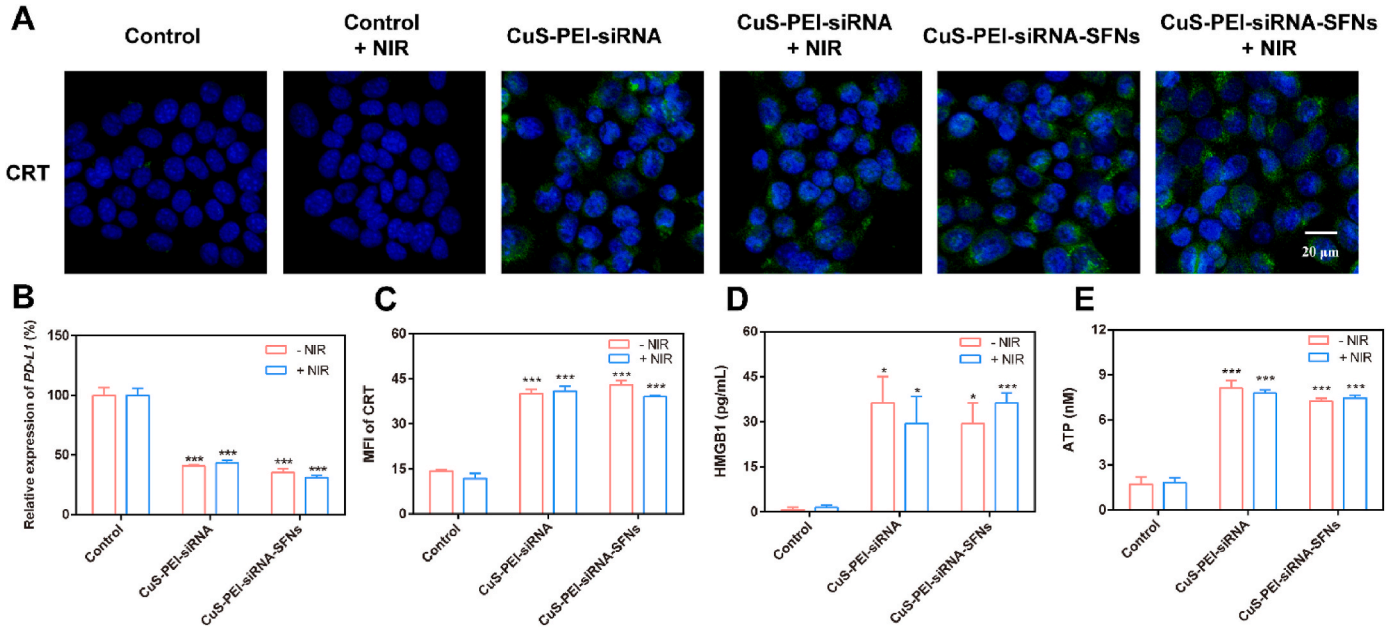

Fig. 6. *PD-L1* gene silencing and immune activation *in vitro*. (A) The immunofluorescence analysis of the CRT (green) exposure and MFI quantitative analysis (C) in the 4T1 cells after different treatments. (B) The *PD-L1* gene expression differences in the 4T1 cells after incubation with different preparations. (D and E) The HMGB1 and ATP levels in the 4T1 cell supernatant obtained using ATP assay and HMGB1 ELISA kits, respectively. The error bars represent the mean ± S.E.M (*P < 0.05, **P < 0.01, and ***P < 0.001, n = 3).

and 31.1 %, respectively. With or without NIR irradiation, the gene silencing effect of the CuS-PEI-siRNA-SFNs-treated group on *PD-L1* was higher than CuS-PEI-siRNA. This result may be due to the protection provided by the SF shell to the siRNA, preventing degradation and increasing efficiency.

ICD is a form of regulated cell death that enhances immunogenicity via various mechanisms, activating the antitumor immune system. Furthermore, this study examined the impact of different preparations on 4T1 cells ICD. The ICD was determined by the extracellular secretion of damage-associated molecular patterns (DAMPs). DAMPs mainly include the cell membrane exposure of calreticulin (CRT) and the extracellular secretion of high-mobility group 1 (HMGB1) and ATP [35, 36]. The CRT exposure on the cell membrane was detected via immunofluorescence. As shown in Fig. 6A, no obvious CRT fluorescence was evident on the 4T1 cell surfaces without NP treatment. However, the outer 4T1 cell surface treated with CuS-PEI-siRNA showed obvious fluorescence. The CuS-PEI-siRNA-SFNs-treated group exhibited stronger CRT fluorescence on the extracellular surface. The quantitative analysis showed that the CRT fluorescence intensity of the CuS-PEI-siRNA-SFNs-treated group was the highest (Fig. 6C). NIR irradiation did not significantly affect the CRT exposure. Further investigation showed that the extracellular HMGB1 and ATP secretion increased dramatically in the CuS-PEI-siRNA-treated and CuS-PEI-siRNA-SFNs-treated groups compared with the control group (Fig. 6D and **E**). Moreover, the intracellular ATP content in the CuS-PEI-siRNA and CuS-PEI-siRNA-SFNs treatment groups was significantly lower than in the control group. Therefore, CuS-PEI-siRNA and CuS-PEI-siRNA-SFNs substantially affected ICD.

3.6. The in vivo biodistribution and photothermal imaging of the NPs

Mice with 4T1 carcinoma xenografts were established to determine whether CuS-PEI-siRNA-SFNs preferentially accumulate in tumors. CuS-PEI-siRNA-SFNs were labeled using NIR dye Cy7 (CuS-PEI-siRNA-Cy7-SFNs) via the reaction between the NHS of Cy7-NHS and the amino of the SF in CuS-PEI-siRNA-SFNs to visualize the NP distribution. The CuS-PEI-siRNA-Cy7-SFNs suspensions were injected intravenously into the mice and subjected to NIR imaging at predetermined time points (6 h, 12 h, 24 h, 48 h, and 72 h). As shown in Fig. 7A, the CuS-PEI-siRNA-Cy7-SFNs accumulated in the tumor tissues after the 6-h injection, effectively penetrating the tumor tissues where they were internalized by the tumor cells. At 6–72 h after injection, the CuS-PEI-siRNA-Cy7-SFNs concentration at the tumor site increased initially, followed by a decrease, exhibiting good accumulation and retention characteristics in the

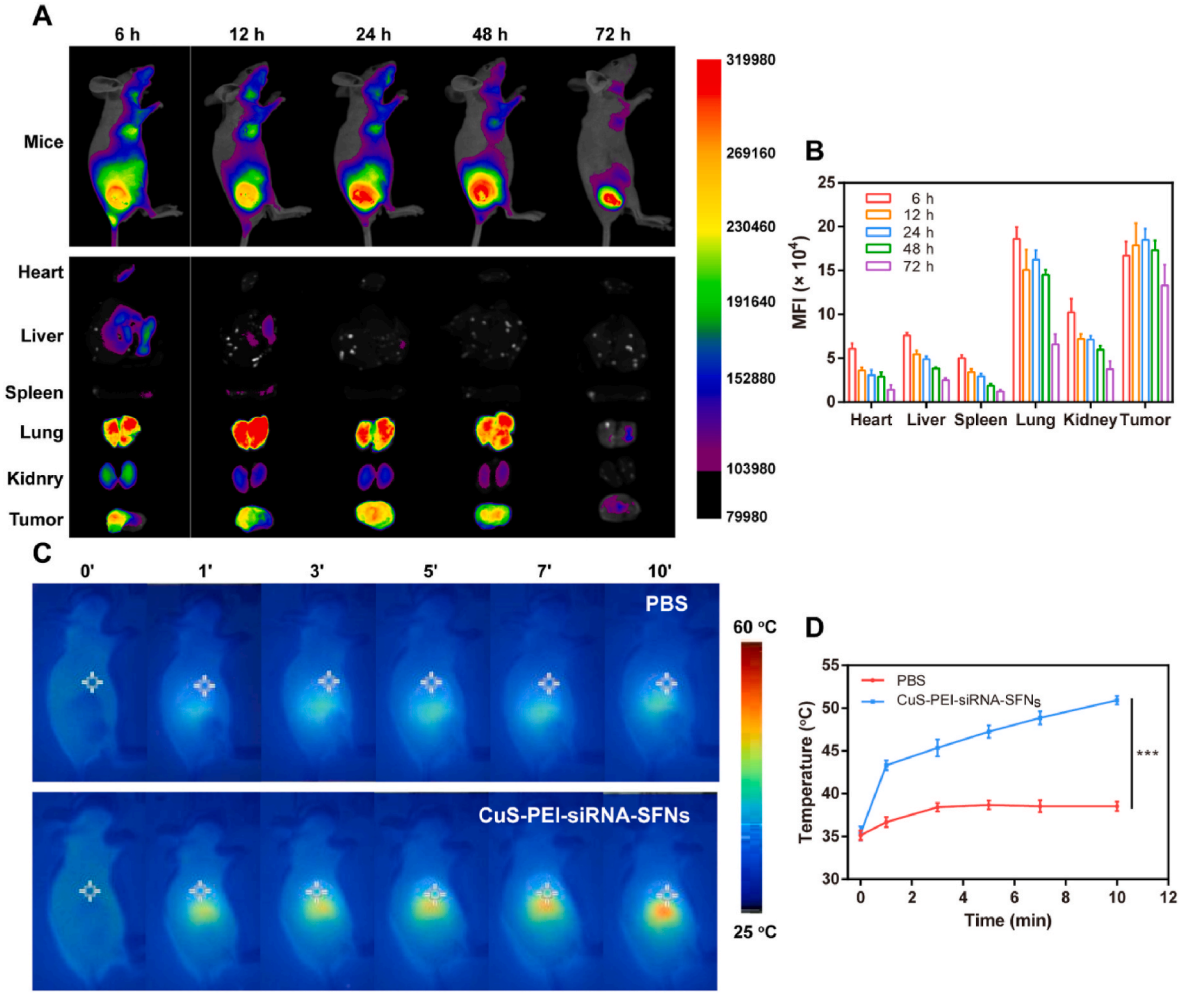

Fig. 7. The *in vivo* biodistribution of the CuS-PEI-siRNA-SFNs in mice bearing 4T1 carcinoma xenografts. (A) The representative fluorescence images of the 4T1 tumor-bearing mice. Five major organs and tumors after exposure to CuS-PEI-siRNA-Cy7-SFNs suspensions at different time points (6 h, 12 h, 24 h, 48 h, and 72 h). (B) The MFIs of the major organs and tumor tissues of the mice after intravenous injection treatment at different time points (6 h, 12 h, 24 h, 48 h, and 72 h). (C) The photothermal images of the 4T1 tumor-bearing mice after the intravenous injection of PBS or CuS-PEI-siRNA-SFNs suspensions at 24 h upon laser irradiation (10 min, 0.8 W/cm^2). (D) The temperature variations in the tumors monitored using an infrared thermal camera. The error bars represent the mean ± S.E.M (***$P < 0.001$, n = 3).

tumors. At 24 h after injection, the fluorescence intensity of CuS-PEI-siRNA-Cy7-SFNs was the highest in the tumors, and the accumulation peaked. Therefore, NIR irradiation was performed 24 h after injecting the mice when the PTT was optimal. Moreover, *ex vivo* imaging of anatomical organs and tumors (Fig.7A) showed that the CuS-PEI-siRNA-Cy7-SFNs preferentially accumulated in the tumors and lungs. The accumulated fluorescence in the major organs and tumor tissues (Fig. 7B) indicated high CuS-PEI-siRNA-Cy7-SFNs levels in the tumors, exceeding those in other major organs at 72 h post-injection. Since 4T1 breast cancer was prone to lung metastasis, the considerable CuS-PEI-siRNA-Cy7-SFNs accumulation in the lungs significantly inhibited lung metastasis. In addition, CuS-PEI-siRNA-Cy7-SFNs in major organs and the fluorescence intensity decreased with an increase in time, reducing the toxic side effects in the organs. This specific CuS-PEI-siRNA-SFNs accumulation in the tumors could be attributed to the passive targeting of enhanced permeability and retention (EPR) effects [37,38]. These results suggest that CuS-PEI-siRNA-Cy7-SFNs can target tumor tissues and remain there for long periods without affecting other organ tissues.

A NIR camera was used to determine the photothermal effect of the CuS-PEI-siRNA-SFNs after intravenous injection at 24 h. As shown in Fig. 7C and **D**, the tumor temperature in the PBS-treated control group stabilized 5 min after irradiation. Contrarily, the tumor temperature of the CuS-PEI-siRNA-SFNs-treated group increased dramatically to 43.3 °C after 1 min of irradiation, indicating a distinct photothermal effect. After 3 min and 5 min of irradiation, the tumor temperature in the CuS-PEI-siRNA-SFNs-treated group increased to 45.4 °C and 47.3 °C, respectively. After 10 min of irradiation, the tumor temperature in the CuS-PEI-siRNA-SFNs-treated group rose to 50.9 °C, significantly exceeding that of the PBS-treated group at 38.5 °C (Fig. 7D). Irradiation and a temperature below 45 °C indicated mild PTT, causing less normal tissue damage. A local average temperature of about 53 °C eliminated tumor cells and inhibited tumor growth without causing irreversible burn injury [39–41]. Therefore, the mild photothermal treatment produced by CuS-PEI-siRNA-SFNs was relatively safe. These results indicated that CuS-PEI-siRNA-SFNs targeted tumor tissue and prolonged detention in tumor, promoting their use for PTT.

3.7. The in vivo anticancer outcomes

To determine the anticancer outcomes of the different treatment strategies, the 4T1 tumor-bearing mice were randomly divided into eight groups: the PBS control group, the PBS (+NIR) control group, the CuS-treated group, the CuS (+NIR)-treated group, the CuS-PEI-siRNA-treated group, the CuS-PEI-siRNA (+NIR)-treated group, the CuS-PEI-siRNA-SFNs-treated group, and the CuS-PEI-siRNA-SFNs (+NIR)-treated group. As shown in Fig. S14, no significant body weight changes were evident in the mice after different treatments compared to the PBS control group. The body weights of the mice in each group increased, indicating a positive response to the treatments. Fig. 8B shows the tumor volume changes in the mice in each treatment group over time. The tumor volumes in the PBS and PBS (+NIR) control groups were significantly higher than the other treatment groups throughout the experiment. Compared with the PBS (±NIR) control groups, CuS (±NIR), CuS-PEI-siRNA (±NIR), and CuS PEI-siRNA-SFNs treatment inhibited tumor volume growth, with the CuS-PEI-siRNA-SFNs (+NIR)-treated group exhibiting the best performance. The tumor growth curve of the CuS-PEI-siRNA-SFNs (+NIR)-treated group differed significantly from the other groups. The antitumor effect in the CuS-treated group was primarily due to the cuproptosis caused by Cu release. As shown in Fig. 8G, the CuS-treated group significantly down-regulated the expression of the cuproptosis marker gene *FDX1* compared with the PBS control group. Similarly, the *FDX1* gene expression was significantly down-regulated in the remaining five treatment groups, indicating that they all triggered cuproptosis. Compared with the CuS and CuS-PEI-siRNA treatment groups, CuS-PEI-siRNA-SFNs treatment showed a stronger antitumor ability due to slow Cu release and the protection provided by the SF shell to siPD-L1, stimulating the immune response to tumors. As shown in Fig. 8H, the *PD-L1* gene expression in the CuS-PEI-siRNA-SFNs-treated group (71.5 %) was significantly lower than in the PBS control group (100 %) and the CuS-PEI-siRNA-treated group (80.9 %). In addition, CuS-PEI-siRNA-SFNs (+NIR) treatment showed a better antitumor ability than CuS-PEI-siRNA-SFNs due to the synergistic effect of ROS generation and photothermal warming on tumors after NIR irradiation, which was mediated by cuproptosis. The average tumor weights obtained via each treatment strategy (Fig. 8D) and the corresponding digital photos of the excised tumors (Fig. S13) were collected at the end of the experiment. The CuS-PEI-siRNA-SFNs (+NIR)-treated group yielded the smallest tumor sizes and average tumor weight (0.3 g) and the highest tumor inhibition rate (56.0 %) (Fig. 8I), confirming that this treatment approach displayed the strongest anticancer effect.

The PBS (±NIR) control groups showed significant pulmonary metastatic tumor nodules due to easy 4T1 breast cancer metastasis (Fig. 8E), showing 30.3 and 30.7 pulmonary metastatic nodules in the PBS and PBS (+NIR) control groups, respectively. CuS (±NIR) and CuS-PEI-siRNA (±NIR) treatment reduced the number of pulmonary metastatic nodules. However, the lungs of the mice in the CuS-PEI-siRNA-SFNs (±NIR)-treated group displayed minimal metastatic nodes. The number of lung metastatic nodules was lowest in the CuS-PEI-siRNA-SFNs (+NIR)-treated group (7.0), which was consistent with the antitumor performance of this strategy. The H&E-stained lung sections (Fig. S16B) confirmed significant malignant transformation in the control groups, while showing the least metastatic lung nodules in the CuS-PEI-siRNA-SFNs (+NIR)-treated group, which was consistent with the quantitative results shown in Fig. 8F. At the end of the experiment, the Cu content in the major organs and tumor tissues of the mice in PBS control, CuS (+NIR)-treated, and CuS-PEI-siRNA-SFNs (+NIR)-treated groups were collected and counted (Figs. 8C and S15). The Cu content in lungs and tumor tissues of the CuS (+NIR)-treated and CuS-PEI-siRNA-SFNs (+NIR)-treated groups were significantly higher than in the PBS control group. This confirmed that CuS (+NIR) and CuS-PEI-siRNA-SFNs (+NIR) treatment inhibited tumor growth via cuproptosis. Moreover, the Cu content in the lungs and tumor tissues of the CuS-PEI-siRNA-SFNs (+NIR)-treated group was significantly higher than in the CuS (+NIR)-treated group since the CuS-PEI-siRNA-SFNs sustained Cu release over an extended period compared with CuS.

To reveal the potential mechanism behind tumor growth inhibition, TUNEL staining was used to detect tumor tissue apoptosis, while the tumor proliferation ability was determined via Ki67 staining. Apoptosis was negligible in the PBS (±NIR) control groups (Fig. S16D). TUNEL green fluorescence was found in the tumor tissues of the other treatment groups. The tumor tissue in the CuS-PEI-siRNA-SFNs (+NIR)-treated group showed the strongest apoptotic fluorescence signal (Fig. S16J), while the positive Ki67 levels were significantly lower than in the other treatment groups (Figs. S16C and S16I**)**. Furthermore, the H&E-stained tumor sections (Fig. S16A) showed that the tumor damage was most severe in the CuS-PEI-siRNA-SFNs (+NIR)-treated group. The role of siPD-L1 in the NP in the tumor tissues was further explored via PD-L1 immunohistochemistry. As shown in Figs. S16E and S16K, PD-L1 was significantly down-regulated in the tumor tissues of the CuS-PEI-siRNA-SFNs (±NIR)-treated group and was lower than in the CuS (±NIR)-treated and CuS-PEI-siRNA (±NIR)-treated groups. In the absence of siPD-L1, the PD-L1 level did not change significantly in the tumor tissues of the CuS (±NIR)-treated group, while it was slightly down-regulated in the CuS-PEI-siRNA (±NIR)-treated group. The PD-L1 level in the CuS-PEI-siRNA-SFNs (±NIR)-treated group was lower than in the CuS-PEI-siRNA (±NIR)-treated group, possibly due to the easy siRNA degradation in the CuS-PEI-siRNA after entering the body, while the SF shell played a protective role. Immunofluorescence staining was performed to evaluate the *in vivo* effect of the different treatments on the tumor immune microenvironment. As shown in Figs. S16F, S16G, and S16H**,** the CRT expression in the tumor tissues of the CuS-PEI-siRNA-SFNs (±NIR)-treated group was significantly higher than in the CuS (±NIR)-treated

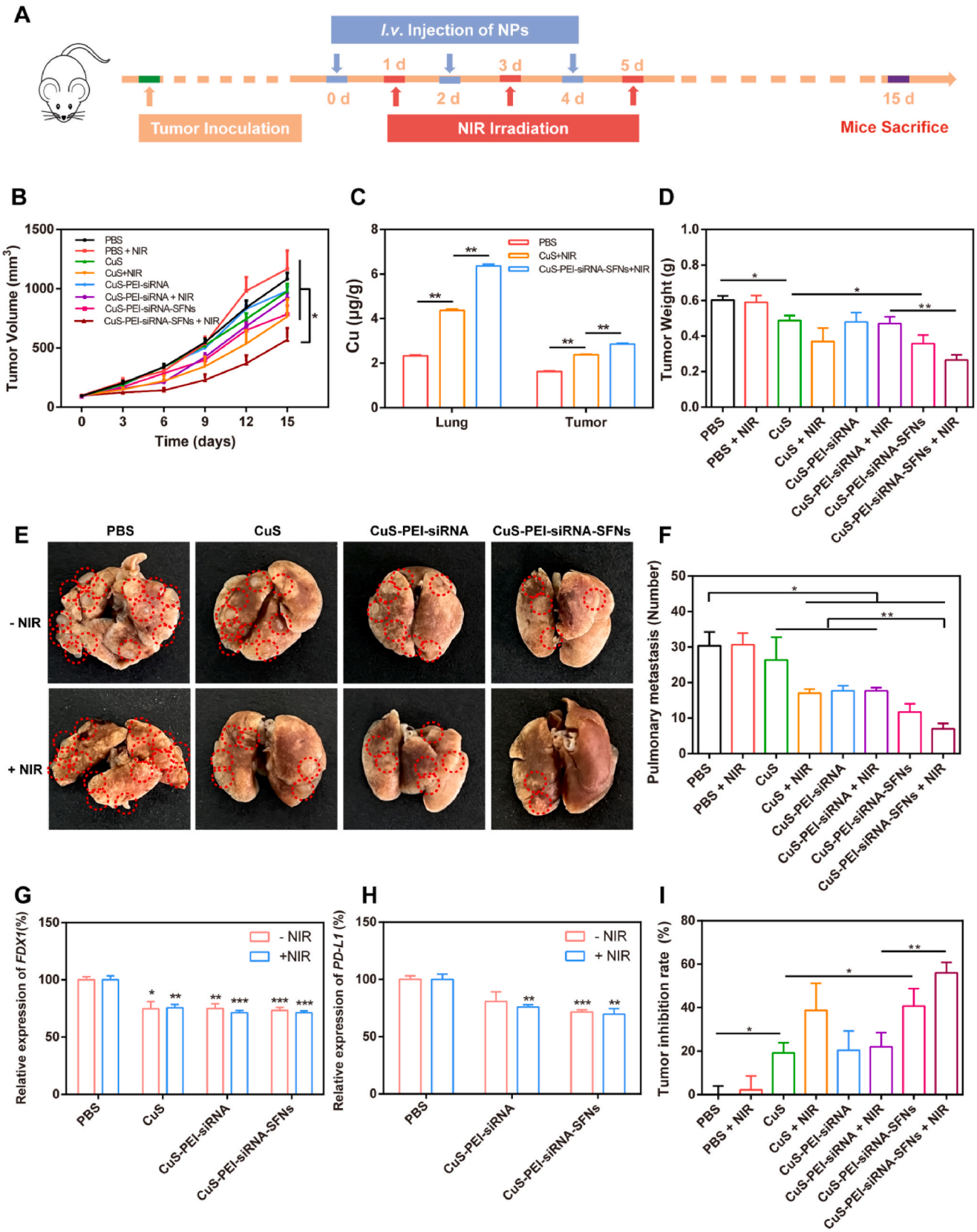

Fig. 8. The *in vivo* therapeutic effect of the various NPs. (A) A schematic illustration of the treatment processes. (B) The tumor growth curves of the mice in the different groups exposed to various treatment strategies. (C) The *in vivo* Cu biodistribution in the different treatment groups at 15 d. (D and I) The tumor weights and inhibition rates in the various treatment groups at 15 d. (E) The images of the mouse lungs in the different treatment groups at 15 d. The red circles indicate the metastatic tumor sites. (F) The number of pulmonary metastatic nodules. (G and H) The *FDX1* and *PD-L1* gene expression differences in the tumors of the different treatment groups at 15 d. The error bars represent the mean ± S.E.M (*$P < 0.05$, **$P < 0.01$, and ***$P < 0.001$, n = 3).

and CuS-PEI-siRNA (±NIR)-treated groups. The quantitative CRT fluorescence results of each treatment group (Fig. S16L) also showed that the CuS-PEI-siRNA-SFNs (±NIR)-treated group exhibited the best ICD effect. When immunotherapy is activated, helper T lymphocytes ($CD4^+$ T cells) and cytotoxic T lymphocytes ($CD8^+$ T cells) are vital for the immune regulation of the tumor microenvironment [29,42,43]. The tumor invasion characteristics of these T lymphocytes were evaluated accordingly. Compared with the PBS (±NIR) control group, no significant changes were evident in the CD4 and CD8 fluorescence in the CuS (±NIR)-treated group, indicating that CuS or irradiation alone could not effectively activate the immune response. The CD4 and CD8 fluorescence increased significantly in the CuS-PEI-siRNA (±NIR)-treated group, indicating partial T lymphocyte infiltration in the tumors. The CD4 and CD8 fluorescence was significantly enhanced in the CuS-PEI-siRNA-SFNs (±NIR)-treated group, indicating that the presence of the SF shell allowed the NPs to stimulate the immune response and reshape the immunosuppressive tumor microenvironment into an immune-supported TME. The immune activation of $CD4^+$/$CD8^+$ T cells was beneficial to inhibiting lung metastasis. Furthermore, no significant differences were evident between the PD-L1, CRT, CD4, and CD8 detection results of the + NIR and - NIR groups, indicating that PTT did not inhibit tumor growth via these mechanisms, and was more conducive to synergistic tumor treatment by multiple mechanisms. These findings suggest that the CuS-PEI-siRNA-SFNs (+NIR)-treated group can achieve antitumor efficacy via multi-mechanism synergy between cuproptosis, PTT, CDT, and immune activation.

Biosafety is essential when treating cancer using nanomedicine. A hemolysis test showed that CuS exhibited obvious hemolysis at a rate of 49.1 % when containing the same amount of Cu (100 μg/mL). This suggests severe hemolytic toxicity may occur if CuS is used in clinical therapy. Contrarily, the CuS-PEI-siRNA-SFNs hemolysis rate was negligible at only 0.2 %. The CuS-PEI-siRNA-SFNs exhibited better blood compatibility than CuS (Fig. S17). The weights of the mice in each treatment group were monitored throughout the experiment and showed a gradual increase (Fig. S14). The whole blood count results showed no significant differences between the 15 indexes in the groups, including the white blood cell count (WBC), lymphocytes (Lymph), monocytes (Mon), neutrophils (Gran), red blood cell count (RBC), hemoglobin (HGB), and platelet count (PLT) (Fig. S18). The biochemical blood indexes were further tested, showing no significant differences between the four liver and kidney function indicators of the treatment groups, including alanine aminotransferase (ALT), aspartate aminotransferase (AST), creatinine (CREA), and urea nitrogen (UREA) (Fig. S19). Analysis of the H&E sections of the administration groups showed no significant histopathological changes in the major organs (hearts, livers, spleens, and kidneys) in each group (Fig. S20). Therefore, the results confirmed the safety of CuS-PEI-siRNA-SFNs *in vivo*.

4. Conclusions

This study constructs a new type of nanoplatform that can induce cuproptosis with multiple PTT, CDT, and immune activation mechanisms. Although CuS shows excellent cuproptosis, PTT, and ROS production ability, it produces hemolytic toxicity. Not only does the CuS-PEI-siRNA-SFNs SF shell protect the siPD-L1, which is conducive to immune activation, but it also realizes long-term slow Cu release and is not prone to hemolysis. In addition, CuS-PEI-siRNA-SFNs show certain selective inhibitory cytotoxicity to normal and tumor cells *in vitro*. CuS-PEI-siRNA-SFNs can effectively target tumor tissues and remain there for extended periods *in vivo*, significantly inhibiting tumor growth and lung metastasis while showing less enrichment and higher safety in other organ tissues. The combined application of quadruple-modal therapeutic strategies (cuproptosis, PTT, CDT, and immune activation) can achieve a synergistic therapeutic effect and improve the anticancer ability of the nanosystem. This multifunctional nanoplatform for cuproptosis induction may provide new approaches for metastatic breast cancer treatment.

CRediT authorship contribution statement

Zheng Li: Writing – original draft, Visualization, Methodology, Investigation, Formal analysis, Data curation, Conceptualization. **Lan Cheng:** Writing – original draft, Visualization, Methodology, Funding acquisition, Formal analysis. **Xiang Xu:** Visualization, Methodology. **Rui Jia:** Validation, Investigation, Formal analysis. **Siyu Zhu:** Validation, Investigation, Data curation. **Qian Zhang:** Investigation, Formal analysis, Data curation. **Guotao Cheng:** Writing – review & editing, Methodology. **Baiqing Wu:** Resources, Investigation. **Zulan Liu:** Writing – review & editing, Funding acquisition. **Xiaoling Tong:** Writing – review & editing. **Bo Xiao:** Writing – review & editing, Supervision, Resources, Project administration. **Fangyin Dai:** Writing – review & editing, Project administration, Funding acquisition, Conceptualization.

Declaration of competing interest

The authors declare the following financial interests/personal relationships which may be considered as potential competing interests.

Acknowledgments

The research was supported by the National Natural Science Foundation of China (No. 32102613), the Natural Science Foundation of Chongqing, China (No. cstc2021jcyj-cxtt0005), the Funds of China Agriculture Research System of MOF and MARA (No. CARS-18-ZJ0102), the Innovation and Entrepreneurship Training Program of Southwest University (No. S202110635237), the Doctor 'Through train' Scientific Research Project of Chongqing (No. CSTB2022BSXM-JSX0019), and the Fundamental Research Funds for the Central Universities under Grant No. SWU120063.

Appendix A. Supplementary data

Supplementary data to this article can be found online at https://doi.org/10.1016/j.mtbio.2024.101298.

Data availability

Data will be made available on request.

References

[1] T. Lang, W. Ran, X. Dong, Z. Zheng, Y. Liu, Q. Yin, Y. Li, Tumor cells-selective bionic nanodevice exploiting heparanase combats metastatic breast cancer, Adv. Funct. Mater. 28 (17) (2018) 1707289.
[2] R.L. Siegel, K.D. Miller, N.S. Wagle, A. Jemal, Cancer statistics, 2023, CA A Cancer J. Clin. 73 (1) (2023) 17–48.
[3] J. Gligorov, S. Richard, Weekly paclitaxel—still preferred first-line taxane for mBC, Nat. Rev. Clin. Oncol. 12 (9) (2015) 508–509.
[4] Y. Huang, D. Xie, S. Gou, B.S.B. Canup, G. Zhang, F. Dai, C. Li, B. Xiao, Quadruple-responsive nanoparticle-mediated targeted combination chemotherapy for metastatic breast cancer, Nanoscale 13 (11) (2021) 5765–5779.
[5] Peter Tsvetkov, Shannon Coy, Boryana Petrova, Margaret Dreishpoon, Ana Verma, Mai Abdusamad, Jordan Rossen, Lena Joesch-Cohen, Ranad Humeidi, Ryan D. Spangler, John K. Eaton, Evgeni Frenkel, Mustafa Kocak, Steven M. Corsello, Svetlana Lutsenko, Naama Kanarek, Sandro Santagata, T.R. Golub, Copper induces cell death by targeting lipoylated TCA cycle proteins, Science 375 (6586) (2022) 1254–1261.
[6] Y. Xu, S.Y. Liu, L. Zeng, H. Ma, Y. Zhang, H. Yang, Y. Liu, S. Fang, J. Zhao, Y. Xu, C. R. Ashby, Y. He, Z. Dai, Y. Pan, An enzyme-engineered nonporous copper(I) coordination polymer nanoplatform for cuproptosis-based synergistic cancer therapy, Adv. Mater. 34 (43) (2022) 2204733.
[7] Y. Lu, Q. Pan, W. Gao, Y. Pu, B. He, Reversal of cisplatin chemotherapy resistance by glutathione-resistant copper-based nanomedicine via cuproptosis, J. Mater. Chem. B 10 (33) (2022) 6296–6306.
[8] F. Hu, J. Huang, T. Bing, W. Mou, D. Li, H. Zhang, Y. Chen, Q. Jin, Stimulus-responsive copper complex nanoparticles induce cuproptosis for augmented cancer immunotherapy, Adv. Sci. 11 (13) (2024) e2309388.

[9] S. Lu, Y. Li, Y. Yu, Glutathione-scavenging celastrol-Cu nanoparticles induce self-amplified cuproptosis for augmented cancer immunotherapy, Adv. Mater. 36 (35) (2024) e2404971.
[10] J. Bai, Y. Liu, X. Jiang, Multifunctional PEG-GO/CuS nanocomposites for near-infrared chemo-photothermal therapy, Biomaterials 35 (22) (2014) 5805–5813.
[11] S. Wang, A. Riedinger, H. Li, C. Fu, H. Liu, L. Li, T. Liu, L. Tan, M.J. Barthel, G. Pugliese, F. De Donato, M. Scotto D'Abbusco, X. Meng, L. Manna, H. Meng, T. Pellegrino, Plasmonic copper sulfide nanocrystals exhibiting near-infrared photothermal and photodynamic therapeutic effects, ACS Nano 9 (2) (2015) 1788–1800.
[12] Y.-N. Chang, M. Zhang, L. Xia, J. Zhang, G. Xing, The toxic effects and mechanisms of CuO and ZnO nanoparticles, Materials 5 (12) (2012) 2850–2871.
[13] K. Jakubczyk, K. Dec, J. Kałduńska, D. Kawczuga, J. Kochman, K. Janda, Reactive oxygen species - sources, functions, oxidative damage, Polski merkuriusz lekarski, organ Polskiego Towarzystwa Lekarskiego 48 (284) (2020) 124–127.
[14] A. Rani, K. Saini, F. Bast, S. Mehariya, S. Bhatia, R. Lavecchia, A. Zuorro, Microorganisms: a potential source of bioactive molecules for antioxidant applications, Molecules 26 (4) (2021) 1142.
[15] M.H. Moustafa, R.K. Sharma, J. Thornton, E. Mascha, M.A. Abdel-Hafez, A. J. Thomas Jr., A. Agarwal, Relationship between ROS production, apoptosis and DNA denaturation in spermatozoa from patients examined for infertility, Hum. Reprod. (Oxf.) 19 (1) (2004) 129–138.
[16] K. Dong, Z. Liu, Z. Li, J. Ren, X. Qu, Hydrophobic anticancer drug delivery by a 980 nm laser-driven photothermal vehicle for efficient synergistic therapy of cancer cells in vivo, Adv. Mater. 25 (32) (2013) 4452–4458.
[17] L. Guo, D.D. Yan, D. Yang, Y. Li, X. Wang, O. Zalewski, B. Yan, W. Lu, Combinatorial photothermal and immuno cancer therapy using chitosan-coated hollow copper sulfide nanoparticles, ACS Nano 8 (6) (2014) 5670–5681.
[18] J. Majidpoor, K. Mortezaee, The efficacy of PD-1/PD-L1 blockade in cold cancers and future perspectives, Clin. Immunol. 226 (2021) 108707.
[19] D.T. Pham, W. Tiyaboonchai, Fibroin nanoparticles: a promising drug delivery system, Drug Deliv. 27 (1) (2020) 431–448.
[20] S. Gou, J. Yang, Y. Ma, X. Zhang, M. Zu, T. Kang, S. Liu, B. Ke, B. Xiao, Multi-responsive nanococktails with programmable targeting capacity for imaging-guided mitochondrial phototherapy combined with chemotherapy, J. Contr. Release : official journal of the Controlled Release Society 327 (2020) 371–383.
[21] S.Q. Gou, Y.M. Huang, Y. Wan, Y. Ma, X. Zhou, X.L. Tong, J. Huang, Y.J. Kang, G. Q. Pan, F.Y. Dai, B. Xiao, Multi-bioresponsive silk fibroin-based nanoparticles with on-demand cytoplasmic drug release capacity for CD44-targeted alleviation of ulcerative colitis, Biomaterials 212 (2019) 39–54.
[22] Q. Li, L. Sun, M. Hou, Q. Chen, R. Yang, L. Zhang, Z. Xu, Y. Kang, P. Xue, Phase-Change Material Packaged within Hollow Copper Sulfide Nanoparticles Carrying Doxorubicin and Chlorin e6 for Fluorescence-Guided Trimodal Therapy of Cancer, ACS Appl. Mater. Interfaces 11 (1) (2018) 417–429.
[23] L. Guo, I. Panderi, D.D. Yan, K. Szulak, Y. Li, Y.T. Chen, H. Ma, D.B. Niesen, N. Seeram, A. Ahmed, B. Yan, D. Pantazatos, W. Lu, A comparative study of hollow copper sulfide nanoparticles and hollow gold nanospheres on degradability and toxicity, ACS Nano 7 (10) (2013) 8780–8793.
[24] Y. Li, M. Cupo, L. Guo, J. Scott, Y.-T. Chen, B. Yan, W. Lu, Enhanced reactive oxygen species through direct copper sulfide nanoparticle-doxorubicin complexation, Nanotechnology 28 (50) (2017) 505101.
[25] Z.J. Deng, S.W. Morton, E. Ben-Akiva, E.C. Dreaden, K.E. Shopsowitz, P. T. Hammond, Layer-by-layer nanoparticles for systemic codelivery of an anticancer drug and siRNA for potential triple-negative breast cancer treatment, ACS Nano 7 (11) (2013) 9571–9584.
[26] H. Fujimoto, K. Kato, H. Iwata, Layer-by-layer assembly of small interfering RNA and poly(ethyleneimine) for substrate-mediated electroporation with high efficiency, Anal. Bioanal. Chem. 397 (2) (2010) 571–578.
[27] Y. Ma, B.S.B. Canup, X. Tong, F. Dai, B. Xiao, Multi-responsive silk fibroin-based nanoparticles for drug delivery, Front. Chem. 8 (2020) 585077.
[28] Z. Li, G. Cheng, Q. Zhang, W. Wu, Y. Zhang, B. Wu, Z. Liu, X. Tong, B. Xiao, L. Cheng, F. Dai, PX478-loaded silk fibroin nanoparticles reverse multidrug resistance by inhibiting the hypoxia-inducible factor, Int. J. Biol. Macromol. 222 (2022) 2309–2317.
[29] X. Zhang, Q. He, J. Sun, H. Gong, Y. Cao, L. Duan, S. Yi, B. Ying, B. Xiao, Near-infrared-enpowered nanomotor-mediated targeted chemotherapy and mitochondrial phototherapy to boost systematic antitumor immunity, Adv. Healthcare Mater. 11 (14) (2022) 2200255.
[30] Z. Zhao, Y. Li, M.B. Xie, Silk fibroin-based nanoparticles for drug delivery, Int. J. Mol. Sci. 16 (3) (2015) 4880–4903.
[31] Q. Feng, W. Zhang, Y. Li, X. Yang, Y. Hao, H. Zhang, W. Li, L. Hou, Z. Zhang, An intelligent NIR-responsive chelate copper-based anticancer nanoplatform for synergistic tumor targeted chemo-phototherapy, Nanoscale 9 (40) (2017) 15685–15695.
[32] S. Zhang, Z. Zha, X. Yue, X. Liang, Z. Dai, Gadolinium-chelate functionalized copper sulphide as a nanotheranostic agent for MR imaging and photothermal destruction of cancer cells, Chem. Commun. 49 (60) (2013) 6776.
[33] F. Chen, H. Hong, S. Goel, S.A. Graves, H. Orbay, E.B. Ehlerding, S. Shi, C. P. Theuer, R.J. Nickles, W. Cai, In vivo tumor vasculature targeting of CuS@MSN based theranostic nanomedicine, ACS Nano 9 (4) (2015) 3926–3934.
[34] K.F. Chu, D.E. Dupuy, Thermal ablation of tumours: biological mechanisms and advances in therapy, Nat. Rev. Cancer 14 (3) (2014) 199–208.
[35] P. Zhang, C. Qin, N. Liu, X. Zhou, X. Chu, F. Lv, Y. Gu, L. Yin, J. Liu, J. Zhou, M. Huo, The programmed site-specific delivery of LY3200882 and PD-L1 siRNA boosts immunotherapy for triple-negative breast cancer by remodeling tumor microenvironment, Biomaterials 284 (2022) 121518.
[36] F. Zhou, B. Feng, H. Yu, D. Wang, T. Wang, Y. Ma, S. Wang, Y. Li, Tumor microenvironment-activatable prodrug vesicles for nanoenabled cancer chemoimmunotherapy combining immunogenic cell death induction and CD47 blockade, Adv. Mater. 31 (14) (2019) 1805888.
[37] Y. Shi, R. van der Meel, X. Chen, T. Lammers, The EPR effect and beyond: strategies to improve tumor targeting and cancer nanomedicine treatment efficacy, Theranostics 10 (17) (2020) 7921–7924.
[38] M. Ikeda-Imafuku, L.L.-W. Wang, D. Rodrigues, S. Shaha, Z. Zhao, S. Mitragotri, Strategies to improve the EPR effect: a mechanistic perspective and clinical translation, J. Contr. Release 345 (2022) 512–536.
[39] Q. Lei, D. He, L. Ding, F. Kong, P. He, J. Huang, J. Guo, C.J. Brinker, G. Luo, W. Zhu, Y. Yu, Microneedle patches integrated with biomineralized melanin nanoparticles for simultaneous skin tumor photothermal therapy and wound healing, Adv. Funct. Mater. 32 (22) (2022) 2113269.
[40] S. Zhang, L. Jin, J. Liu, Y. Liu, T. Zhang, Y. Zhao, N. Yin, R. Niu, X. Li, D. Xue, S. Song, Y. Wang, H. Zhang, Boosting chemodynamic therapy by the synergistic effect of Co-catalyze and photothermal effect triggered by the second near-infrared light, Nano-Micro Lett. 12 (1) (2020).
[41] P. Xue, R. Yang, L. Sun, Q. Li, L. Zhang, Z. Xu, Y. Kang, Indocyanine green-conjugated magnetic prussian blue nanoparticles for synchronous photothermal/photodynamic tumor therapy, Nano-Micro Lett. 10 (4) (2018).
[42] B. Farhood, M. Najafi, K. Mortezaee, CD8+ cytotoxic T lymphocytes in cancer immunotherapy: a review, J. Cell. Physiol. 234 (6) (2018) 8509–8521.
[43] X. Liu, M. Shen, T. Bing, X. Zhang, Y. Li, Q. Cai, X. Yang, Y. Yu, A bioactive injectable hydrogel regulates tumor metastasis and wound healing for melanoma via NIR-light triggered hyperthermia, Adv. Sci. 11 (26) (2024) e2402208.